Nanoscale

PAPER

View Article Online
View Journal | View Issue

Cite this: *Nanoscale*, 2021, **13**, 2931

A high-energy-density supercapacitor with multi-shelled nickel–manganese selenide hollow spheres as cathode and double-shell nickel–iron selenide hollow spheres as anode electrodes†

Akbar Mohammadi Zardkhoshoui,* Bahareh Ameri and Saied Saeed Hosseiny Davarani *

Thanks to the attractive structural characteristics and unique physicochemical properties, mixed metal selenides (MMSes) can be considered as encouraging electrode materials for energy storage devices. Herein, a straightforward and efficient approach is used to construct multi-shelled nickel–manganese selenide hollow spheres (MSNMSeHSs) as cathode and double-shell nickel–iron selenide hollow spheres (DSNFSeHSs) as anode electrode materials by tuning shell numbers for supercapacitors. The as-designed MSNMSeHS electrode can deliver a splendid capacity of ~339.2 mA h g^{-1}/1221.1 C g^{-1}, impressive rate performances of 78.8%, and considerable longevity of 95.7%. The considerable performance is also observed for the DSNFSeHS electrode with a capacity of 258.4 mA h g^{-1}/930.25 C g^{-1}, rate performance of 75.5%, and longevity of 90.9%. An efficient asymmetric apparatus (MSNMSeHS||DSNFSeHS) fabricated by these two electrodes depicts the excellent electrochemical features (energy density of ≈112.6 W h kg^{-1} at 900.8 W kg^{-1}) with desirable longevity of ≈94.4%.

Received 18th November 2020,
Accepted 30th December 2020

DOI: 10.1039/d0nr08234a

rsc.li/nanoscale

1. Introduction

Driven by the ever-increasing market development in mobile electronic and electric vehicles, the demand for cost-effective and highly efficient energy storage devices (ESDs) has been continually increasing in last two decades.[1,2] Among different high-efficiency ESDs, supercapacitors (SCs) have been widely utilized in portable electronics, biomedical devices, and various renewable energy systems due to their notable features, including significant robustness, environment-friendly, good safety, and desirable power density.[3–7] Despite the considerable power capabilities of SCs, the main impediment for its practical utilization is its inherently low energy densities. To elevate the energy density of supercapacitors, which is estimated employing this equation (ED = $1/2CV^2$), either the cell voltage (V) or capacity (C) needs to be enhanced.[8,9] A possible strategy to improve C is to substitute pseudocapacitance electrode materials with electrochemical double-layer capacitor materials (EDLC) since pseudocapacitive materials reflect high capacitance in comparison to EDLCs.[10,11] On the other side, the cell voltage (V) is also a crucial factor in lifting the ED of supercapacitors. A useful route to boost the cell voltage is producing asymmetric devices.[12,13]

During last few years, a wide spectrum of pseudocapacitance materials has been designed as promising electrode materials for SCs, including metal oxides,[14] sulfides,[15] and selenides.[16] Among these electrode materials, metal selenides such as NiSe,[17] $FeSe_2$,[18] $CoSe_2$,[19] and $MoSe_2$[20] have received particular attention as a proper candidate by virtue of their intrinsic desired conductivity. Recently, MMSes with mixture phases of various metal selenides illustrated higher conductivity and richer redox reactions compared to single-component metal selenides, indicating their inherent advantages for charge storage. Among them, nickel-based mixed selenides (such as Ni–Mn–Se, Ni–Co–Se, and Ni–Fe–Se) come into the limelight owing to the high redox properties of nickel.[21–23] However, the fabrication of Ni–Mn- or Ni–Fe-based mixed metal selenides was rarely reported.

While different metal selenides have been extensively investigated as positive-electrodes in asymmetric devices, EDLC carbon materials were conventionally used as the negative electrode.[24,25] Unfortunately, the low specific capacitance of

Department of Chemistry, Shahid Beheshti University, G. C., 1983963113, Evin, Tehran, Iran. E-mail: ss-hosseiny@sbu.ac.ir, mohammadi.bahadoran@gmail.com; Fax: +98 21 22431661; Tel: +98 21 22431661

†Electronic supplementary information (ESI) available: Supplementary characterization and electrochemical data, and a benchmark table to compare the performance of the as-prepared device with previously reported devices. See DOI: 10.1039/d0nr08234a

EDLC carbon materials limits the application of asymmetric supercapacitors. Accordingly, the quest for preparing novel pseudocapacitive negative electrodes with high capacity is crucial, and could be highly beneficial in lifting the ED of devices. One alternative is using Fe-based materials as a pseudocapacitor negative electrode because of the low cost, natural abundance, and low toxicity of iron.[21,22] Nevertheless, their low surface area (SA) and conductivity are the main drawbacks in improving the performance of SCs. Different approaches can be used to address these defects. The first approach is to enhance the electrical conductivity by selecting mixed metal selenides instead of mixed metal oxide/sulfides and/or single metal selenides.[21,22] The second approach is using structural engineering to design electrode materials with a high surface area.[26] Inspired by these, nickel–iron selenide (NFSe) is an encouraging negative electrode due to the high electrical conductivity. However, few studies have elucidated the nanostructuring effects on improving its performance.

It is well-reported that the structural complexity of materials can effectively boost the longevity and rate capability of electrode materials.[26,27] Among the different possible designs, hollow nanostructures with complex architecture seem to be promising thanks to their structure-dependent merits.[28,29] Considering the supercapacitor applications, complex hollow architectures present significant advantages over simple hollow structures. Intricate hollow structures inherit the features of hollow constructions such as the large electrode/electrolyte interface, high surface area, and enhanced volume change accommodation, which together with improved weight fraction of the species, can provide a high-energy density.[30,31]

In the current paper, we introduce a straightforward approach to synthesize multi-shelled nickel–manganese selenide hollow spheres (MSNMSeHSs) and double-shell nickel–iron selenide hollow spheres (DSNFSeHSs) with an adjustable number of shells. In a three-electrode system, the MSNMSeHS electrode depicted a splendid capacity of 339.2 mA h g^{-1}/1221.1 C g^{-1}, and exceptional longevity of 95.7%, and the DSNFSeHS electrode reflected a high capacity of 258.4 mA h g^{-1}/930.25 C g^{-1} and desired cyclability of 90.9%. Interestingly, these two electrodes can be assembled as a MSNMSeHS||DSNFSeHS asymmetric apparatus, resulting in high capacity (125.1 mA h g^{-1}/450.36 C g^{-1}), splendid energy/power densities (112.6 W h kg^{-1}/900.8 W kg^{-1}), along with an amazing longevity of 94.4%.

2. Experimental details

2.1 Materials

To fabricate the electrode materials, the chemicals were Ni$(CH_3COO)_2{\cdot}4H_2O$ [nickel(II) acetate tetrahydrate], glucose, Mn$(CH_3COO)_2{\cdot}4H_2O$ [manganese(II) acetate tetrahydrate], C_2H_6O [ethanol], SeO_2 [selenium dioxide], $C_2H_6O_2$ [ethylene glycol], $N_2H_4{\cdot}H_2O$ [hydrazine monohydrate], $FeCl_3{\cdot}6H_2O$ [iron(III) chloride hexahydrate], and CH_3COONH_4 [ammonium acetate].

2.2 Synthesis of the MSNMSeHS sample

In a typical preparation, Ni$(CH_3COO)_2{\cdot}4H_2O$ (0.02 mol), glucose (0.05 mol), and Mn$(CH_3COO)_2{\cdot}4H_2O$ (0.02 mol) were completely dissolved in the distilled water (100 mL) under stirring for 15 min. Subsequently, the mixture was transferred into a suitable Teflon tank, sealed in the autoclave, and heated at 180 °C for 7 h. After cooling at an ordinary temperature, the black precipitate was carefully collected, washed, and then centrifuged by water and ethanol four times. The as-made powder was dried for 12 h at 70 °C, and then collected as a precursor. Next, the multi-shelled Ni–Mn oxide hollow spheres were fabricated by annealing the collected precursors in the air at 500 °C for 1.5 h with a ramping rate of 1 °C min^{-1}. Also, the morphology evolution of the Ni–Mn oxide as a function of calcination time (*e.g.*, 0.5, 1, and 1.5 h) was further evaluated at the constant temperature, as well as the constant ramping rate. Next, SeO_2 (0.5 mmol) was added to ethylene glycol (15 mL). After that, $N_2H_4{\cdot}H_2O$ (5 mL) was added to this solution. Then, 39 mg of the as-fabricated MSNMOHS sample was added to the solution under stirring. After stirring for about 1 h, our mixture was put into the autoclave and kept for 6 h at 180 °C. The black precipitate was carefully filtered, rinsed adequately with water and ethanol, and dried for further characterization.

2.3 Synthesis of the DSNFSeHS sample

Typically, $FeCl_3{\cdot}6H_2O$ (270.3 mg) and Ni$(CH_3COO)_2{\cdot}4H_2O$ (248.8 mg), and CH_3COONH_4 (0.5 g) were completely dissolved into ethylene glycol (40 mL) to form the solution. The solution was carefully transferred into an autoclave, and then kept at 180 °C for 10 h in the oven. The precursor was well collected using centrifugation after it completely cooled down to ambient temperature. Next, the collected powder was annealed at 400 °C in the air at different calcination times from 0.5 h to 1.5 h at a constant heating rate of 1 °C min^{-1} to precisely control the morphology. The same method for the preparation of MSNMSeHS was carefully followed to fabricate the DSNFSeHS sample.

2.4 Characterization

The morphologies and comprehensive structural information of the as-made products were well characterized by employing field-emission SEM (FE-SEM: TESCAN: Mira IIILMU: Czech Republic) and TEM (Philips CM200 instrument). The chemical valence states and crystal structures of the fabricated samples were also analyzed by XPS (Thermo Scientific/ESCALAB 250Xi Mg X-ray source) and XRD ((Philips X'pert diffractometer). The specific surface areas (SSA) and pore diameter distribution of the MSNMSeHS and DSNFSeHS samples were obtained through the N_2 adsorption/desorption test (Micromeritics ASAP 2010) by the Brunauer–Emmett–Teller (BET) and Barret–Joyner–Halenda (BJH) methods.

2.5 Electrochemical evaluation

Electrochemical experiments were performed at an environmental temperature in both two-electrode and three-electrode

configurations by employing EIS, GCD, and CV tests. In a three-electrode configuration, KOH (6 M solution), Ag/AgCl, and Pt plate were applied as the proper electrolyte, reference, and counter electrodes, respectively. The working electrodes were prepared with 85% of the collected powders, 10% of acetylene black, and 5% of polyvinylidene fluoride in acetone. Then, the obtained paste was pressed onto the nickel foam (NF) and completely dried at 70 °C for 24 h. The specific capacities (Cs: mA h g^{-1}/C g^{-1}) of the as-made electrodes were achieved *via* the following two eqn (1) and (2):[32,33]

$$\mathrm{Cs}\ (\mathrm{C\,g^{-1}}) = \frac{I \times \Delta t}{m} \quad (1)$$

$$\mathrm{Cs}\ (\mathrm{mA\,h\,g^{-1}}) = \frac{I \times \Delta t}{3.6 \times m} \quad (2)$$

where Δt (s) specifies the discharge time, m (g) denotes the mass of the as-prepared electroactive materials on the substrate surface, and I (A) presents the current density. In addition, an effective apparatus (MSNMSeHS||DSNFSeHS) was easily constructed by using the MSNMSeHS (cathode electrode) and DSNFSeHS (anode electrode) as a promising alternative for activated carbon. The total charge contained in the cathode and anode electrodes in a MSNMSeHS||DSNFSeHS apparatus must be consistent ($q+ = q-$). The equation for estimating the charge per electrode is as follows:[34]

$$q = Q \times m \quad (3)$$

where Q (C g^{-1}) indicates the capacity of the electrode and m (g) specifies the mass of the electroactive material. Therefore, the mass of the cathode electrode and anode electrode were tuned based on the following equation:[34]

$$\frac{m+}{m-} = \frac{Q-}{Q+} \quad (4)$$

where $Q+$ and $m+$ are the capacity and mass of the MSNMSeHS electrode material, respectively. $Q-$ and $m-$ are the capacity and mass of the DSNFSeHS electrode material, respectively.

According to eqn (4), the specific mass utilized to constructed the MSNMSeHS||DSNFSeHS device was ~2.6 mg cm^{-2} and ~3.4 mg cm^{-2} for the MSNMSeHS and DSNFSeHS electrodes, respectively. Besides, the coulombic efficiency of all electrodes can be evaluated from the formula CE = $t_D/t_C \times 100\%$, where t_C and t_D are the galvanostatic charging and discharging times. As for the energy density (ED) and power density (PD) of the MSNMSeHS||DSNFSeHS apparatus, they were calculated by utilizing the following equations:[32–34]

$$\mathrm{ED}\ (\mathrm{W\,h\,kg^{-1}}) = \frac{CV^2}{7.2} \quad (5)$$

$$\mathrm{PD}\ (\mathrm{W\,kg^{-1}}) = \frac{\mathrm{ED} \times 3600}{\Delta t}. \quad (6)$$

3. Results and discussion

3.1 Formation mechanism of the MSNMSeHS

The usual synthesis of the multi-shelled structures is time-consuming and complicated, and requires processes such as ion adsorption, template removal, and template synthesis.[35–37] In contrast, we developed an appropriate way to prepare multi-shelled structures with an adjustable number of shells with the aid of metal acetate polysaccharides (MAPs) as the promising self-template (Fig. 1a). The MSNMSeHS sample with an obvious gap between neighboring thin shells is fabricated using a hydrothermal route and thermal treatment, followed by selenization. A homogeneous solution from glucose and metal acetates is fabricated for the hydrothermal reaction. During the polymerization of glucose, metal cations (Mn^{2+}, and Ni^{2+}) are effectively adsorbed over the polysaccharides to create metal acetate polysaccharides (MAPs) *via* the coordinating process that includes the intermolecular dehydration of glucose and concurrent coordination of metal ions.[38] The adsorbed transition metal ions (Ni^{2+} and Mn^{2+}) on the MAPs' skeleton will further reinforce the growth of spheres by playing a role as the cross-linking agent, and making coordination bonds by free-flowing glucose. This leads to carbonaceous spheres with a rigid nature (FE-SEM, TEM images and schematic image in Fig. 1b1–b3). During the annealing of the metal acetate polysaccharides in air, the rigid structures began to shrink at around 500 °C for 0.5 h, and the surfaces of the spheres were converted into the metal oxide shell, which was obtained by the high-temperature gradient (Fig. 1c1–c3). In this context, two fundamental forces, the adhesion force and contraction force, are acting concurrently on the shell interfaces in opposing directions. The contraction force, which leads to the inward shrinkage of the internal sphere, is caused by the considerable weight reduction throughout the oxidative degradation. On the other hand, the adhesion force prevents the interior contraction of the distinct core from the comparatively rigid shell. At 500 °C for 1 h, the internal carbon sphere with rigid nature relatively decomposes. The nature of the spheres becomes rougher and the outer shell of the spheres did not change, whilst the inner shells gradually formed, as confirmed by the FE-SEM, TEM images and schematic image (Fig. 1d1–d3). At ~500 °C for 1.5 h, multi-shelled nickel–manganese oxide hollow spheres (MSNMOHSs) were produced (Fig. 1e1–e3). Then, the obtained nickel manganese oxide sample was selenized by employing selenide ions from selenium hydrazine solution to generate nickel manganese selenide (Fig. 1f1–f3). The nickel manganese selenide maintains its structure after the selenization process.

3.2 Characterizations of the MSNMSeHS

To investigate the structure and morphology of the products, the FE-SEM and TEM techniques were applied and the collected images are shown in Fig. 2a–h and Fig. S1 (ESI†). An FE-SEM image (Fig. S1†) approved the formation of the metal acetate polysaccharide (MAP) spheres with a smooth surface as precursors. The EDS mapping also demonstrates good element

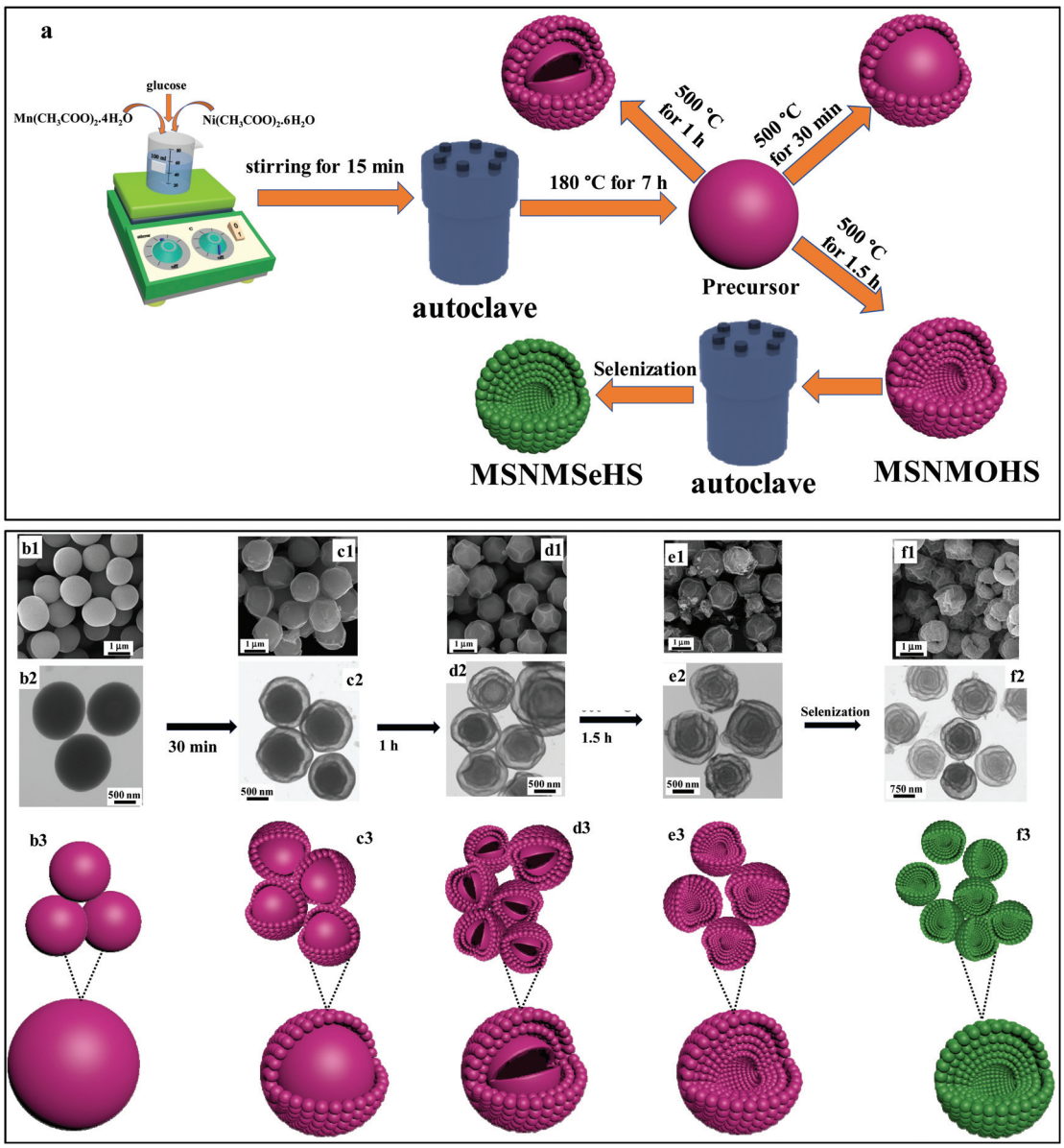

Fig. 1 (a) The schematic fabrication process of the MSNMSeHS. (b1–b3) FE-SEM image, TEM image and the corresponding schematic illustration of the MAPs before thermal treatment. (c1–c3) FE-SEM image, TEM image and the corresponding schematic illustration of the MAPs after thermal treatment at 500 °C for 30 min. (d1–d3) FE-SEM image, TEM image and the corresponding schematic illustration of the MAPs after thermal treatment at 500 °C for 1 h. (e1–e3) FE-SEM image, TEM image and the corresponding schematic illustration of the MAPs after thermal treatment at 500 °C for 1.5 h. (f1–f3) FE-SEM image, TEM image and the corresponding schematic illustration of the MSNMSeHS.

distribution in MAPs (Fig. S2†). Also, a TEM image verifies the rigid nature of the MAPs with a smooth surface (Fig. S3†). From Fig. 2a, it can be viewed that the MSNMSeHS sample retains the spherical skeleton of the MAP precursor well. The FE-SEM image in Fig. 2b suggests that the as-made spheres demonstrate a relatively non-dense and rough surface. Also, the surface of the spheres is made up of plicated petal structures and is well decorated with wrinkles, which help increase the contact area between the electrolyte and material surface (Fig. 2c). The EDS mapping images of the MSNMSeHS sample prove the differentiated distributions of Mn, Ni, and Se throughout the texture of the sample (Fig. 2d1–d4). The formation of MSNMSeHS was also well evaluated using the EDX spectrum, as represented in Fig. 2e, indicating the availability of elements, such as Ni, Mn, and Se with their amount of 31.77, 33.12, and 35.11 atom%, respectively. The TEM method illustrated the interior structures of the MSNMSeHS in detail. As reflected in Fig. 2f and g, the multi-shelled porous structure can be clearly identified through the non-uniform contrasts between the specific shells (dark), as well as the internal cavities (light) of spheres. It is also quite clear from Fig. 2h that the shells are made up of several small nanoparticles, which

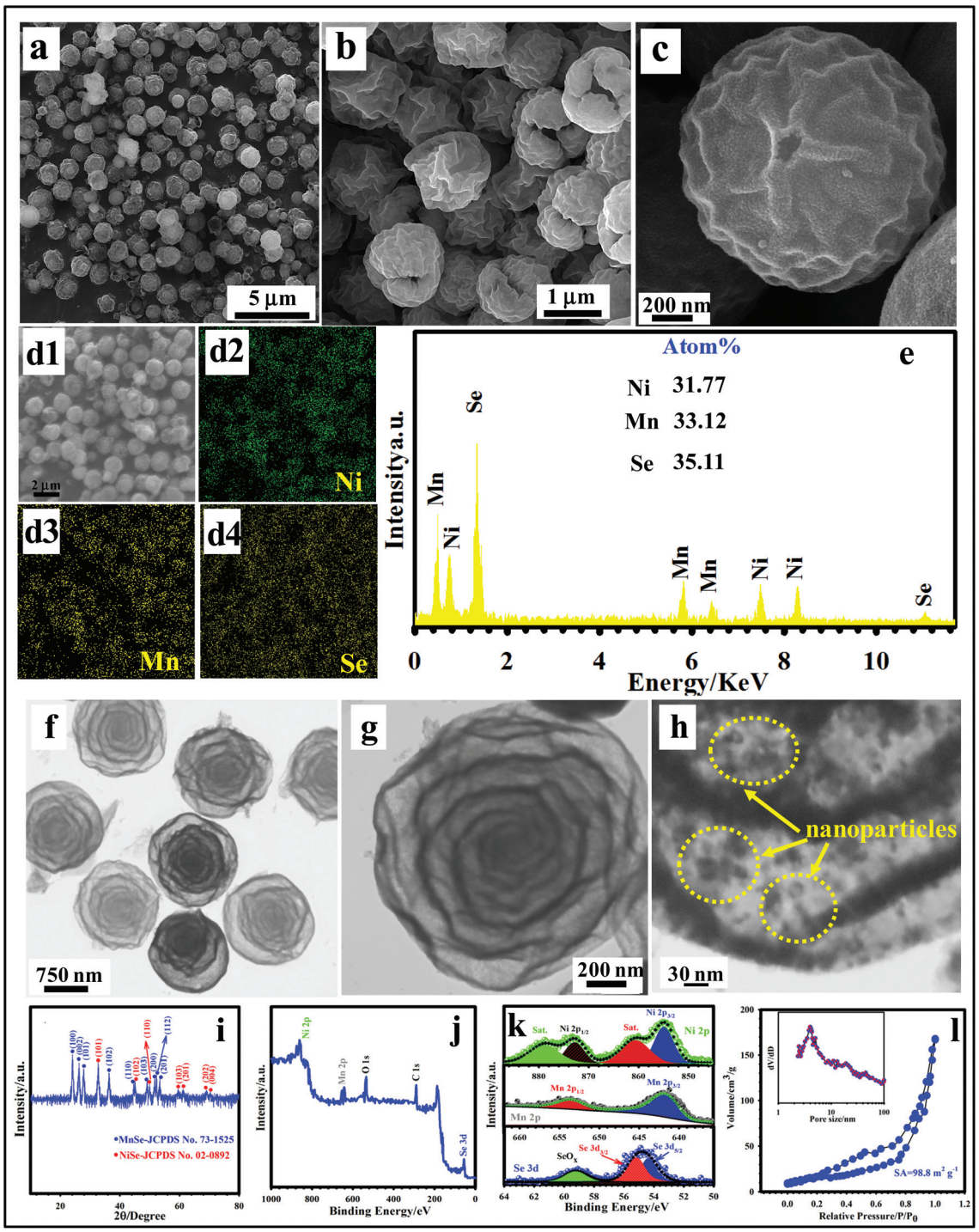

Fig. 2 (a–c) FE-SEM images of MSNMSeHS. (d1–d4) EDS mapping of MSNMSeHS. (e) EDX spectrum of MSNMSeHS. (f–h) TEM images of MSNMSeHS. (i) XRD pattern of MSNMSeHS. (j) Survey spectrum of MSNMSeHS. (k) Ni 2p, Mn 2p, and Se 3d XPS spectra of MSNMSeHS. (l) BET curve of MSNMSeHS and its corresponding BJH plot (inset).

are obtained owing to the thermal conversion of the MAP rigid nanospheres. Such multi-shelled porous structures with rich voids can guarantee the effortless infiltration of the electrolyte from the outer surface to the inside, and also ensure the ions from both inner and outer shell to be transferred.[39,40] Also, these spheres own the desirable specific area, which can offer plentiful active sites. This leads to the best performance in the supercapacitors. To make sure that the target sample (MSNMSeHS) was successfully fabricated, the crystal structure of our product was tested by XRD, and is displayed in Fig. 2i.

As evidenced in Fig. 2i, the MSNMSeHS is constructed from NiSe (JCPDS 02-0892) and MnSe (JCPDS 73-1525). The MnSe demonstrated distinct peaks at ~24.03°, 26.18°, 27.83°, 36.38°, 44.63°, 49.08°, 51.64°, 52.31°, and 53.37°, corresponding to the (100), (002), (101), (102), (110), (103), (200), (112), and (201) planes, respectively.[41,42] Meanwhile, the NiSe displayed noticeable peaks at 32.81° (101), 44.62° (102), 49.95° (110), 59.49° (103), 61.18° (201), 69.048° (202), and 70.38° (004).[43] XPS is another extensively used technique for analyzing the oxidation states of the elements, as well as the surface elemental composition. As evidenced in Fig. 2j, the typical signals for Mn 2p, Ni 2p and Se 3d in the full survey spectrum prove that the fabricated sample comprises the Mn, Ni, and Se species, which is in agreement with the EDX result. It should be noted that the C element in the spectrum arises from the C reference for calibration.[44] As illuminated in the Ni 2p XPS spectrum (Fig. 2k), two principal peaks at 872.77 and 854.95 eV are ascribable to the Ni $2p_{1/2}$ and Ni $2p_{3/2}$, respectively. Moreover, two obvious satellite peaks (identified as "Sat.") at binding energies of 860.58 and 878.59 eV further confirmed the existence of Ni^{2+}.[45] The Mn 2p spectrum is reflected in Fig. 2k, from which two noticeable peaks were detected at 641.5 eV (Mn $2p_{3/2}$) and 653.3 eV (Mn $2p_{1/2}$), which suggest that Mn exists primarily in the Mn^{2+} oxidation state.[46] Fig. 2k reveals the Se 3d XPS, the Se $3d_{5/2}$ peak at 54.68 eV, and the Se $3d_{3/2}$ peak at 55.48 eV, which are features of the metal–selenium (M–Se) bonds. Also, the broad peak at 59.2 eV results from the oxidized Se.[45] The XPS study proves that the MSNMSeHS was successfully fabricated. It is certainly true that the surface area and porous nature of the materials can make a valuable contribution to improve the electrochemical features.[4,10] Accordingly, we assessed the textural features of MSNMSeHS. As evidenced in Fig. 2l, the isotherm of MSNMSeHS depicts a typical IV curve along with an apparent hysteresis loop, signifying the mesoporous nature of the MSNMSeHS with a SA of ≈98.8 $m^2\ g^{-1}$, as well as a pore size of ≈4.6 nm. The porous architecture with a considerable SA can offer copious channels for effective ion electrolyte infiltration, which is valuable for the electrochemical reactions of the nanomaterials.[4,7,10]

3.3 Formation mechanism of DSNFSeHS

Fig. 3a schematically discloses a facile strategy for the fabrication of the DSNFSeHS sample. The formation mechanism investigation of the DSNFSeHS sample was elaborately conducted using FE-SEM, as well as TEM observation to obtain a comprehensive understanding of the formation process of the DSNFSeHS sample. Fig. 3b–f reveals the representative FE-SEM and TEM images, along with a schematic illustration with different calcination times ranging from 0.5 to 1.5 h for Ni–Fe-oxide and the selenization for Ni–Fe-selenide. It can be viewed in Fig. 3b1–b3 that the obtained precursor is made up of rigid spheres without discernible pores. From Fig. 3c1–c3, it can see that a partially hollow nature with a rough surface for spheres is visibly seen just after calcination for 0.5 h. With the extension of the calcination time up to 1 h (Fig. 3d1–d3), there is a large gap space between a porous shell and a rigid yolk, forming an exclusive yolk–shell nanostructure. Remarkably, a unique double-shell hollow structure with a completely hollow cavity can be successfully obtained when the calcination time is increased to 1.5 h, as evidenced in Fig. 3e1–e3. At the time of the selenization reaction, the Se^{2-} ions would react with the surface Fe^{2+}/Ni^{2+} ions of the Ni–Fe-oxide structures *via* ion exchange reaction to fabricate a Ni–Fe–Se sample. Also, the Ni Fe selenide relatively maintains its original texture after the ion exchange reaction (Fig. 3f1–f3).

3.4 Characterizations of DSNFSeHS

The morphology features of DSNFSeHS were well analyzed by using FE-SEM and TEM techniques, as displayed in Fig. 4. The FE-SEM images of DSNFSeHS are represented in Fig. 4a and b, indicating that DSNFSeHS inherits the spherical shape from its precursor, and displays a porous and hollow architecture. An enlarged view (Fig. 4c) shows that the DSNFSeHS sample with a highly rough surface is composed of countless nanoparticles, which can contribute to a great surface area. The distribution of desired elements in DSNFSeHS was examined by EDS mapping analysis. The EDS mapping results (Fig. 4d1–d4) reveal that Fe, Ni, and Se are well distributed in the DSNFSeHS sample. Besides, the formation of DSNFSeHS was investigated by using the EDX spectrum, as reflected in Fig. 4e, revealing the availability of elements, such as Fe, Ni, and Se with their amount of 34.21, 32.57, and 33.22 atom%, respectively. The internal structure of the as-made DSNFSeHS was also elucidated by TEM characterization. As evidenced in Fig. 4f, porous double-shelled structures can be identified for the sample. Besides, a magnified TEM image of the single sphere unambiguously demonstrates that the outer and inner shells of DHNFSeHS both possess a spherical structure with a highly porous texture (Fig. 4g). A high-magnification image (Fig. 4h) demonstrates the emergence of the numerous tiny nanoparticles on the single hollow sphere. Such a porous architecture is expected to demonstrate facilitated charge/mass transport, great surface area, ample active sites, and reduced aggregation of subunits for improved supercapacitive performance.[4,7,10] The identification of the phase formation of the as-made sample is essential, and it was well-analyzed using XRD. As reflected in Fig. 4i, the DSNFSeHS comprised FeSe (JCPDS 75-0608) and NiSe (JCPDS 02-0892). The NiSe revealed distinct peaks at 27.81° (100), 32.77° (101), 44.53° (102), 49.92° (110), 59.52° (103), 61.15° (201), 69.05° (202), and 70.42° (004).[43] At the same time, the FeSe reflected visible peaks at 30.38° (002), 32.13° (101), 42.1° (102), 50.8° (110), 55.78° (103), 61.97° (201), 63.48° (004), 67.63° (202), and 77.65° (203).[47,48] The XPS technique was also applied to demonstrate the successful formation of DSNFSeHS by analyzing its oxidation states. Using the full spectrum (Fig. 4j), it is evident that the Fe, Ni, and Se signals exist in the DSNFSeHS sample. Also, the O and C elements can be well detected in DSNFSeHS, owing to the surface adsorption of oxygen and the impact of the test environment.[47,48] The high-resolution XPS

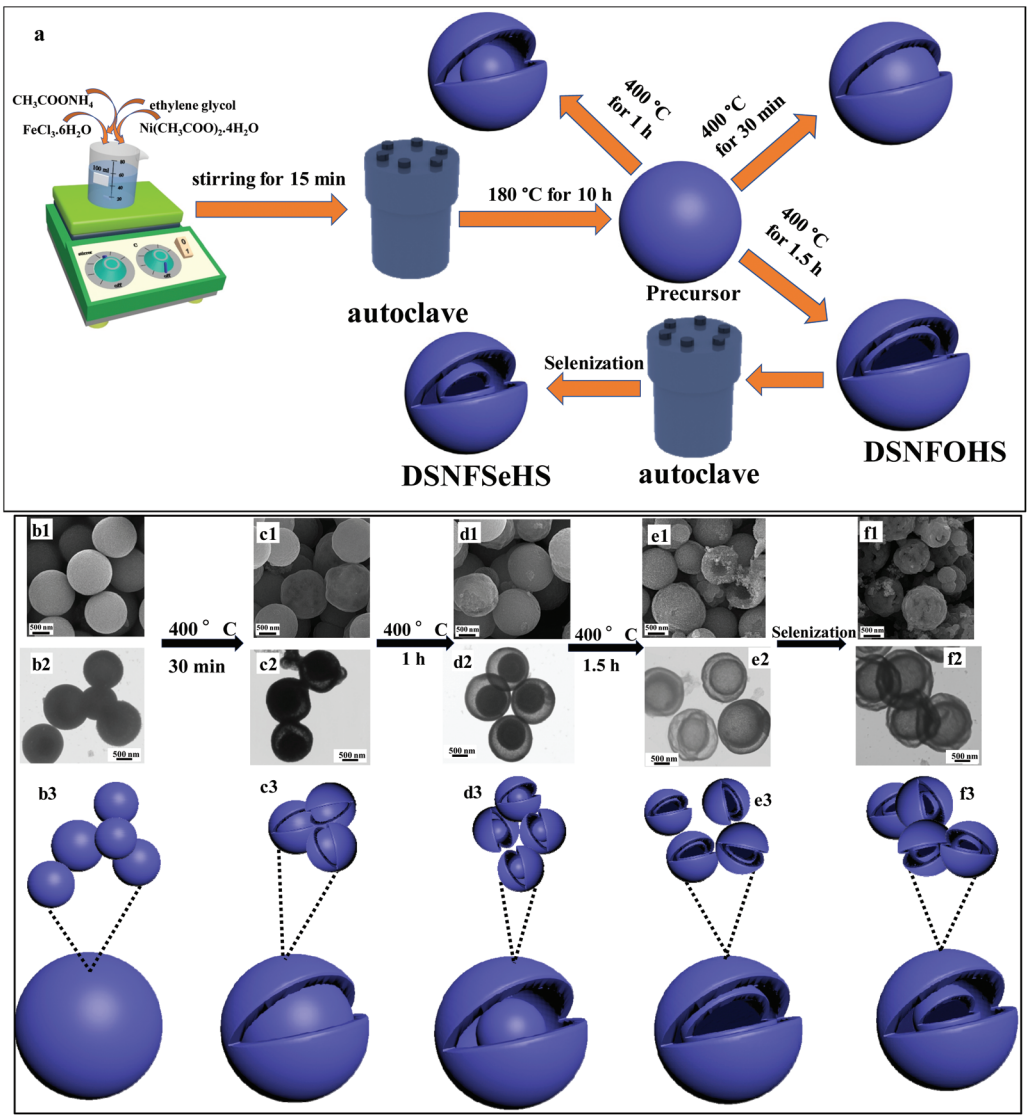

Fig. 3 (a) The schematic fabrication process of DSNFSeHS. (b1–b3) FE-SEM image, TEM image and the corresponding schematic illustration of the precursor before thermal treatment. (c1–c3) FE-SEM image, TEM image and the corresponding schematic illustration of the precursor after thermal treatment at 400 °C for 30 min. (d1–d3) FE-SEM image, TEM image and the corresponding schematic illustration of the precursor after thermal treatment at 400 °C for 1 h. (e1–e3) FE-SEM image, TEM image and the corresponding schematic illustration of the precursor after thermal treatment at 400 °C for 1.5 h. (f1–f3) FE-SEM image, TEM image and the corresponding schematic illustration of DSNFSeHS.

spectra of Fe, Ni, and Se are well fitted by the Gaussian method, as reflected in Fig. 4k. The XPS of Fe 2p in Fig. 4k mainly indicates two wide peaks, and could be well deconvoluted into various components: the obvious peaks at 710.64 and 723.93 eV for Fe^{2+}; the peaks around 719.18 and 727.37 eV represent the satellite peaks; the peaks situated at 713.17 and 725.09 eV for Fe^{3+}, which derive from the partial oxidation of iron selenide by oxygen throughout the sample transfer.[49,50] The Ni 2p spectrum reflected in Fig. 4k consists of distinct peaks placed at 873.38 and 855.78 eV, representing the Ni $2p_{1/2}$ and Ni $2p_{3/2}$ energy levels, respectively. Hence, it is clear from this spectrum that the Ni in the synthesized sample possesses a +2 oxidation state. Also, the other peaks at 861.08 and 879.38 eV were detected as satellite peaks.[51,52] Fig. 4k shows that the XPS of Se 3d consisted of two peaks placed at 55.12 eV (Se $3d_{3/2}$) and 54.22 eV (Se $3d_{5/2}$), which indicates the formation of a metal selenide. Besides, the peak centered at 58.77 eV is assigned to the Se–O bond.[53] To verify the mesoporous nature, as well as determine the SA of the DSNFSeHS sample, BET analysis was conducted (Fig. 4l). Based on the BET analysis, the SA for the DSNFSeHS sample was estimated to be 81.7 $m^2\ g^{-1}$. The pore size distribution (inset in Fig. 4l) of DSNFSeHS shows that the pores in DSNFSeHS are mainly placed at 5.3 nm, illustrating its mesoporous nature.[4,7,10] Accordingly, an enhanced supercapacitive behavior could be expected for the DSNFSeHS sample. This is because the great surface area can offer ample active sites to improve the redox reactions.[4,7]

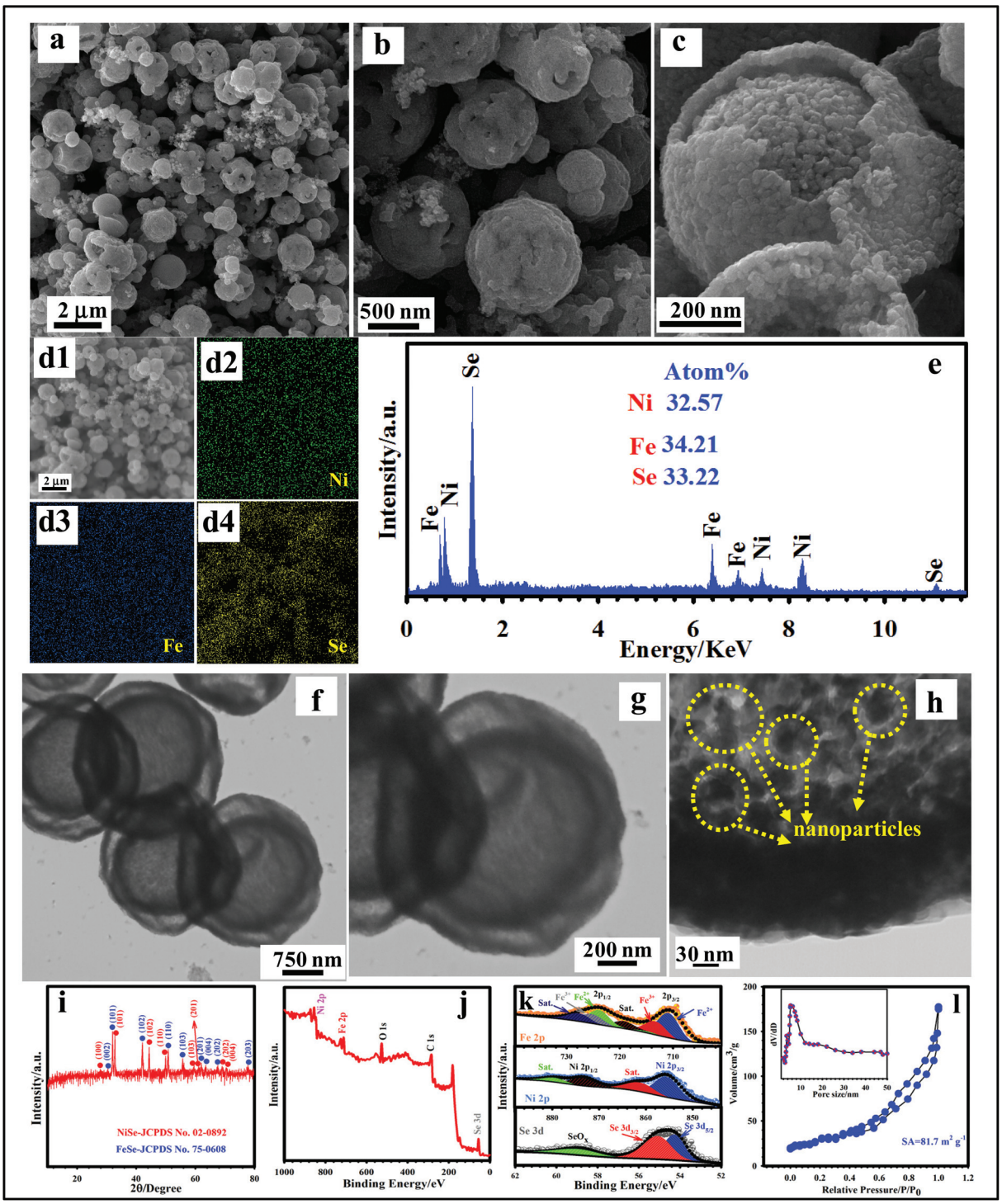

Fig. 4 (a–c) FE-SEM images of DSNFSeHS. (d1–d4) EDS mapping of DSNFSeHS. (e) EDX spectrum of DSNFSeHS. (f–h) TEM images of DSNFSeHS. (i) XRD pattern of DSNFSeHS. (j) Survey spectrum of DSNFSeHS. (k) Ni 2p, Fe 2p, and Se 3d XPS spectra of DSNFSeHS. (l) BET curve of DSNFSeHS and its corresponding BJH plot (inset).

3.5 Electrochemical features of the MSNMSeHS and DSNFSeHS electrodes

To prove the influence of composition optimization and structure design on the supercapacitive behavior, a series of tests were conducted in a three-electrochemical cell using KOH (6 M solution) as an electrolyte. The CV plots of MSNMSeHS, MSNMOHS, and pure NF electrodes at a fixed sweep speed (60 mV s^{-1}) are revealed in Fig. S4a (ESI†). It can be viewed from the CV graphs in Fig. S4a† that the produced current of

pure NF can be ignored compared with that of the MSNMSeHS and MSNMOHS electrodes, proving that the NF substrate has an insignificant contribution to the pseudocapacitance of the MSNMSeHS and MSNMOHS electrodes. It can be certainly discovered that there are a couple of manifest redox peaks with a distinct potential separation in the CVs of the MSNMSeHS and MSNMOHS electrodes. This implies that the as-made MSNMSeHS and MSNMOHS are the battery-type electrodes, and it is substantially different from the CV plots of the EDLC materials with rectangular shapes.[54,55] Most importantly, the MSNMSeHS possesses a larger integral area in comparison with the MSNMOHS electrode, which denotes that the MSNMSeHS electrode has better charge storage performance compared with the MSNMOHS electrode. The reasonable reasons for such results are related to the improvement of the electrical conductivity due to the presence of the Se element in this sample and the logical design of this sample.[4,25] The related redox reactions of the MSNMSeHS electrode in KOH (6 M solution) can be characterized as the following equations:[56–58]

$$\mathrm{NiSe} + \mathrm{OH}^- \leftrightarrow \mathrm{NiSeOH} + \mathrm{e}^- \quad (7)$$

$$\mathrm{MnSe} + \mathrm{OH}^- \leftrightarrow \mathrm{MnSeOH} + \mathrm{e}^- \quad (8)$$

The evaluation of the charge storage capacity of the MSNMSeHS and MSNMOHS electrodes was also done by interpreting the GCD profiles (Fig. S4b†). The nonlinear plots of both samples also verify the battery-like redox nature, which agrees well with the related results from the CV profiles. The highest discharge time was obtained for MSNMSeHS at 2 A g^{-1}, which was predicted from the CV graphs (Fig. S4a†). The discharge time of the MSNMSeHS was about 610 s, and was higher than that for the MSNMOHS electrode (about 517 s). To further explore the underlying reason for the elevated supercapacitive performance of the rationally fabricated MSNMSeHS electrode, the EIS test was performed, as represented in Fig. S4c.† As specified in Fig. S4c,† the Nyquist profiles of the MSNMSeHS and MSNMOHS electrodes represented the common attributes, such as a nearly direct line (low-frequency region) and the depressed semicircle (high-frequency region). These properties are related to the diffusion resistance (Warburg impedance) and the charge-transfer resistance (R_{ct}).[59,60] The R_{ct} value can be estimated from the diameter of the semicircle, and the calculated values are 0.6 Ω for the MSNMSeHS electrode and 0.85 Ω for the MSNMOHS electrode. Also, the R_s (internal resistance) of the MSNMSeHS and MSNMOHS electrodes can be obtained from the intercept of the EIS plot with the *X*-axis, and the values are calculated to be 0.75 and 1.1 for the MSNMSeHS and MSNMOHS electrodes, respectively. The smaller R_s and R_{ct} values for MSNMSeHS further demonstrated its superior electrochemical conductivity, as well as rapid electro-kinetics of the electroactive material.[59,60] Fig. 5a represents the CV profiles of the MSNMSeHS electrode at diverse sweep rates of 10–60 mV s^{-1} in a voltage range of 0–0.60 V. After the CV tests at varied sweep speeds, it can be seen that the reduction and oxidation peaks begin to move toward low and high potential direction with the enhancing of scan speed, respectively. In addition, the respective peak currents improve simultaneously. This phenomenon can be well interpreted by utilizing the concentration polarization theory.[61] Throughout the CV experiments, there will be an increased number of electrons amassed on the surface of the electrodes with the enhancement of the sweep speed. So, the ions in the condensed layer on the electrode surface will be consumed, which results in that the transportation speed of the ions in the diffusion layer cannot follow up with the adsorption/desorption speed of the ions in the condensed layer. Accordingly, it can be deduced that the liquid-phase diffusion processes are the speed-controlling step of the entire reactions. The considerable SA and the ample open space of the multi-shell NiMnSe hollow spheres synthesized in this research, which means a significant number of short pathway diffusion channels, can substantially relieve this process of concentration polarization. Meantime, all of the profiles still preserve their identical shape without any deformation, revealing the splendid rate performance of the MSNMSeHS electrode.[62,63] In contrast, the MSNMOHS electrode was examined at several sweep speeds from 10–60 mV s^{-1}, and its CV plots are represented in Fig. S5.† Fig. 5b depicts the GCD plots for the MSNMSeHS (from 2 to 32 A g^{-1}) electrode. As displayed in Fig. 5b, at all current densities, the MSNMSeHS electrode reflected non-linear shapes, as well as followed a battery-type redox mechanism. Also, all curves represented an almost symmetric nature in the discharging and charging time, justifying the great coulombic efficiency of the MSNMSeHS electrode.[4,10] Besides, the GCD plots of the MSNMOHS electrode under the same current densities in Fig. S6† illustrates that the MSNMOHS electrode has a similar behavior. By utilizing the GCD profiles, the specific capacities for the MSNMSeHS and MSNMOHS electrodes were accurately calculated at various current densities. The calculated capacities at 2, 4, 8, 16, and 32 A g^{-1} for the MSNMSeHS electrode were 339.2 mA h g^{-1} (1221.1 C g^{-1}), 330.9 mA h g^{-1} (1191.25 C g^{-1}), 300.1 mA h g^{-1} (1080.35 C g^{-1}), 285.9 mA h g^{-1} (1029.25 C g^{-1}), and 267.3 mA h g^{-1} (962.3 C g^{-1}), respectively. Meanwhile, the estimated values for the MSNMOHS electrode were 287.3 mA h g^{-1} (1034.3 C g^{-1}), 275.1 mA h g^{-1} (990.35 C g^{-1}), 253.7 mA h g^{-1} (913.3 C g^{-1}), 214.65 mA h g^{-1} (772.75 C g^{-1}), and 200.25 mA h g^{-1} (720.9 C g^{-1}) under the similar current densities. Hence, the MSNMSeHS and MSNMOHS electrodes retained ~78.8% and ~69.7% of the initial specific capacities, respectively, when the current density improved to 32 A g^{-1} (Fig. 5c), implying the good rate performance of the MSNMSeHS and MSNMOHS electrodes. Such a splendid rate capability and an impressive capacity for the MSNMSeHS sample were probably derived from the main factors. It is well established that the hollow architectures with porous shapes, thin shells, and multi-shell-based materials are made up of countless nanoparticles and have a larger surface area. The surfaces of these samples are also composed of interconnected particles, which are more favorable to boost the contact area of the electrodes, and can offer many diffusion

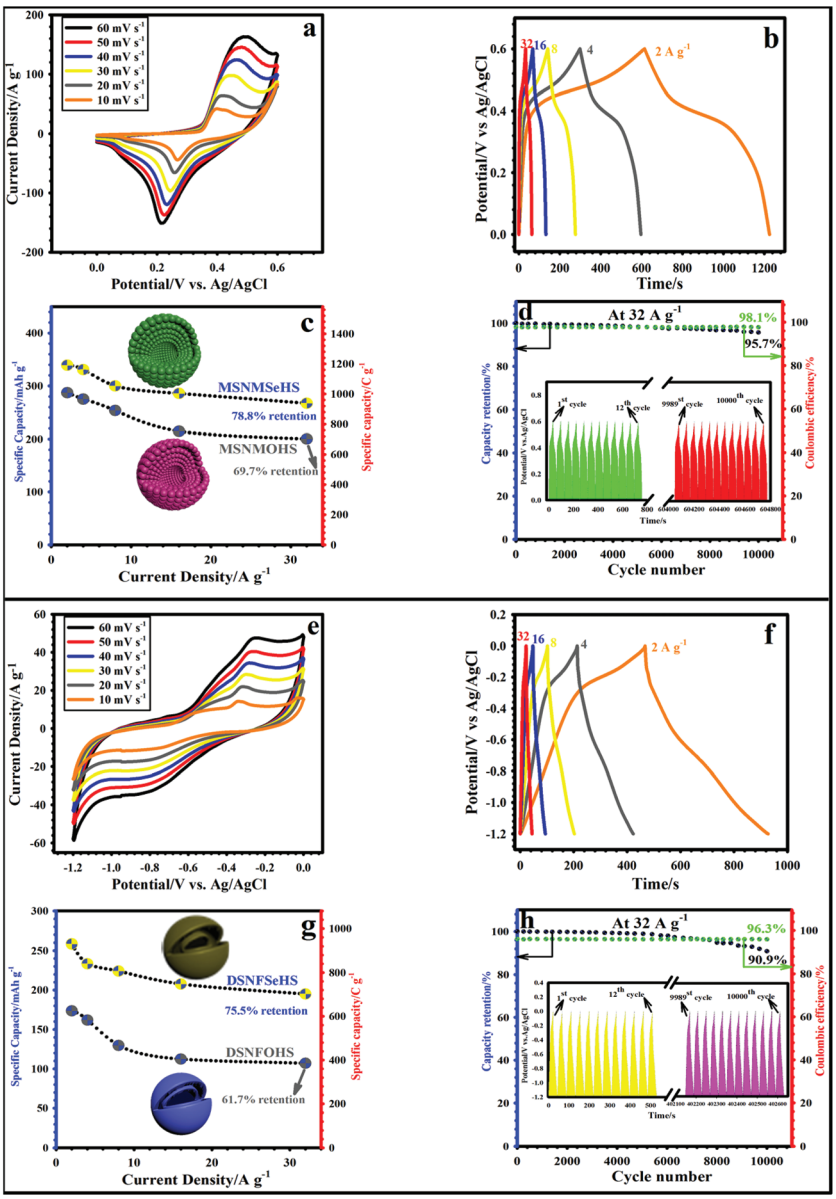

Fig. 5 (a) CV curves of the MSNMSeHS electrode at various sweep rates. (b) GCD profiles of the MSNMSeHS electrode at diverse current densities. (c) Rate capability of the MSNMSeHS and MSNMOHS electrodes. (d) Cyclability and coulombic efficiency of the MSNMSeHS electrode at 32 A g^{-1}. (e) CV curves of the DSNFSeHS electrode at several sweep rates. (f) GCD plots of DSNFSeHS at variant current densities. (g) Rate performance of the DSNFSeHS and DSNFOHS electrodes. (h) Cyclability and coulombic efficiency of the DSNFSeHS electrode at 32 A g^{-1}.

channels for the infiltration of electrolyte ions throughout the electrochemical test.[4,30,64] Based on the BET test, it is well known that the MSNMSeHS sample illustrates a high SA with porous features. A large SA could offer higher active sites, and the porosity offers improved channels for the efficient infiltration of electrolyte ions.[30,64] This can facilitate the charge transportation paths and fast redox reactions to obtain the maximum rate performance and capacity. Since longevity is a decisive requirement for SCs, consecutive GCD tests were done for the MSNMSeHS and MSNMOHS at 32 A g^{-1}, and the related results are reflected in Fig. 5d and Fig. S7.† After the longevity test for 10 000 times, the capacity value of the MSNMSeHS electrode was preserved at ~255.8 mA h g^{-1} (920.9 C g^{-1}) with amazing retention of the capacity of ~95.7% (Fig. 5d). Also, the capacity value of the MSNMOHS electrode was maintained at ~180.03 mA h g^{-1} (648.1 C g^{-1}) with desirable retention of the capacity of ~89.9% (Fig. S7†). The GCD profiles of the MSNMSeHS electrode from the 1st to 12th cycles and plots from 9989st to 10 000th cycles are revealed in Fig. 5d (inset). As evidenced in Fig. 5d, the shape of the last 12 cycles was retained in comparison to the first cycles with minimal change, revealing the amazing longevity of the MSNMSeHS electrode. Moreover, the first and last 12 cycles of the MSNMOHS electrode are indicated in Fig. S7† (inset). The marginal change was identified in the last 12 GCD cycles, reflecting that the MSNMOHS has good longevity. To guaran-

tee the splendid longevity of the MSNMSeHS and MSNMOHS electrodes, the impedance analysis was done before and after the longevity test, as evidenced in Fig. S8a and S8b.† As revealed in Fig. S8a and S8b,† there is no noticeable change in the R_{ct} and R_s values for the MSNMSeHS and MSNMOHS electrodes after 10 000 cycles, displaying the marvelous durability of the MSNMSeHS and MSNMOHS electrodes. To validate the structural durability of the MSNMSeHS sample after the durability test, FE-SEM and TEM analyses were conducted, and the collected images are revealed in Fig. S9.† As demonstrated in Fig. S9,† the images prove that the original structure of the MSNMSeHS sample was well maintained after the durability test, illustrating that the sample has outstanding longevity. The amazing longevity of the MSNMSeHS electrode can arise from the following points: (i) the presence of selenium in the NiMnSe structure can help elevate its interior conductivity, as well as structural stability;[3,4] (ii) the obvious gap between the thin shells can effectively enhance the electrolyte penetration and offer a great contact area between the electrolyte and electrode throughout cycling, thereby enhancing the longevity.[4] Also, we checked the coulombic efficiency of the MSNMSeHS and MSNMOHS electrodes. The MSNMSeHS and MSNMOHS electrodes hold an efficiency of ~98.1% (Fig. 5d) and 94.3% (Fig. S7†) after 10 000 sequential cycles, respectively. The supercapacitive behavior of the MSNMSeHS electrode was better in comparison with the other samples represented in Table S1 (ESI†). The superior supercapacitive performance of the MSNMSeHS compared with the other research studies revealed in Table S1† can be described using the principal reasons, as follows: (i) the development of internal multi-shelled structures with a highly porous skeleton gives an enhanced surface area and a higher number of electroactive sites for charge storage; (ii) the thin shells decorated by nanoparticles shorten the charge-mass transport path; (iii) the certain gap between the formed shells offers the desired hollow space to address the large volume expansion throughout the cycling process. After the good optimization of MSNMSeHS as an encouraging positive electrode, the precise electrochemical characterization was conducted for the DSNFSeHS as a novel negative electrode. Fig. S10a† presents the CV plots of the DSNFSeHS and DSNFOHS electrodes in an operating window of −1.2–0.0 V at a sweep speed of 60 mV s^{-1}. From these plots, DSNFSeHS presented a higher redox current and larger enclosed area than DSNFOHS, signifying its greater energy-storage capacity. It is also evident that a couple of obvious redox peaks were observed in the DSNFSeHS electrode, which signifies the faradaic redox features of the DSNFSeHS electrode. The possible redox reactions under the electrochemical tests for the DSNFSeHS sample can be elucidated as follows:[22,56,57]

$$NiSe + OH^- \leftrightarrow NiSeOH + e^- \quad (9)$$

$$FeSe + OH^- \leftrightarrow FeSeOH + e^- \quad (10)$$

The larger enclosed CV area of DSNFSeHS is mainly ascribed to its higher electrical conductivity owing to the presence of selenium in the sample.[3,4,22] Also, to further assess the supercapacitive behavior for the DSNFSeHS and DSNFOHS electrodes, the GCD test was done. Fig. S10b† reflects the comparative GCD plots of the DSNFSeHS and DSNFOHS electrodes at 2 A g^{-1}. The larger specific area of the DSNFSeHS electrode reflected the longer discharge time as compared to that of DSNFOHS, which can guarantee the splendid specific capacity and agreed with the related CV results. The EIS profiles of the DSNFSeHS and DSNFOHS electrodes were also collected and are represented in Fig. S10c.† The estimated R_s values for the DSNFSeHS and DSNFOHS electrodes were ~0.8 and 1.15 Ω, respectively. Moreover, the R_{ct} values for the DSNFSeHS and DSNFOHS electrodes were estimated to be 0.68, and 0.94 Ω, respectively. Accordingly, the DSNFSeHS sample displayed the lower R_s and R_{ct} values in comparison to the DSNFOHS electrode, which proves the improvement of the redox electrochemistry, as well as desirable conducting behavior of the DSNFSeHS sample. Fig. 5e depicts the related CV profiles of the DSNFSeHS electrode at diverse sweep speeds (10 to 60 mV s^{-1}). The CV shapes of the as-made DSNFSeHS electrode at all sweep speeds illustrated the redox peaks, verifying the battery-type nature of our electrode. From the related CV plots of DSNFSeHS, no substantial change in the peak position and shape was detected with the increment in sweep speed from 10 to 60 mV s^{-1}. This justified the remarkable electrochemical processes at the DSNFSeHS electrode. For comparison, the CVs of the DSNFOHS electrode were recorded from 10 to 60 mV s^{-1}, and the related CVs are plotted in Fig. S11.† Fig. 5f indicates the GCD profiles of the DSNFSeHS electrode from 2 to 32 A g^{-1}. These plots display small plateaus with nearly symmetric shapes. From these profiles, these potential plateaus are similar to the peaks observed in the CV curves, implying the pseudocapacitive behavior in the DSNFSeHS electrode. Moreover, the GCD graphs of the DSNFOHS electrode are revealed in Fig. S12† from 2 to 32 A g^{-1}. As evidenced in Fig. S12,† all collected profiles demonstrated the non-linear nature, which is in excellent agreement with the related CV graphs. The estimated capacity values at 2, 4, 8, 16, and 32 A g^{-1} for the DSNFSeHS electrode were 258.4 mA h g^{-1} (930.25 C g^{-1}), 233.4 mA h g^{-1} (840.25 C g^{-1}), 224.15 mA h g^{-1} (806.95 C g^{-1}), 207.75 mA h g^{-1} (747.9 C g^{-1}), and 195.1 mA h g^{-1} (702.3 C g^{-1}), respectively. Meanwhile, the calculated values for the DSNFOHS electrode were 173.6 mA h g^{-1} (624.95 C g^{-1}), 161.9 mA h g^{-1} (582.85 C g^{-1}), 129.7 mA h g^{-1} (466.9 C g^{-1}), 112.4 mA h g^{-1} (404.65 C g^{-1}), and 107.1 mA h g^{-1} (385.55 C g^{-1}), respectively, under identical conditions. The DSNFSeHS electrode maintains a splendid capacity value of 195.1 mA h g^{-1} (702.3 C g^{-1}) with retention of 75.5%, which is better than that for the DSNFOHS electrode (Fig. 5g). This outstanding capacity and superb rate capability are better than the already reported results, as far as we know (Table S2†). Several underlying causes might be useful for understanding these phenomena. First, the double-shelled Ni–Fe–Se provides a satisfactory surface area, abundant pores, as well as rich channels.[4] Second, its special morphology can make the KOH electrolyte simply engage in the electrochemical redox reactions. Third, the selenium in NiFe–Se may help to enhance its electrical

conductivity.[3,4] The longevity of the DSNFSeHS and DSNFOHS electrodes was checked under 10 000 uninterrupted GCD cycles at 32 A g^{-1} to assess their stabilities. Fig. 5h and Fig. S13† demonstrate the longevity results of the DSNFSeHS and DSNFOHS electrodes, displaying ~90.9 and 85.6% of the capacity retention after uninterrupted 10 000 cycles. The related GCD graphs of the DSNFSeHS electrode from the 1st to 12th GCD cycles and the curves from the 9989th to 10 000th cycles are demonstrated in Fig. 5h (inset). As is evident from Fig. 5h, the shape and nature of the last 12 cycles are well preserved compared with the first GCD curves with an unimportant change, revealing the impressive longevity of the DSNFSeHS electrode. On the other side, the first and last 12 cycles of the DSNFOHS electrode are specified in Fig. S13† (inset). The faint change was recognized in the last 12 cycles, suggesting that DSNFOHS has the desired longevity. Furthermore, to ensure the splendid durability of the DSNFSeHS and DSNFOHS electrodes, the EIS analysis was applied before and after the longevity test, as revealed in Fig. S14a and S14b.† As manifested in Fig. S14a and S14b,† there is no dramatic change in the R_{ct} and R_s values for the DSNFSeHS and DSNFOHS electrodes after the durability test, displaying the splendid durability of the DSNFSeHS and DSNFOHS electrodes. Most importantly, to endorse the structural durability of the DSNFSeHS after the longevity test, FE-SEM and TEM analyses were applied and the related images are displayed in Fig. S15a and S15b.† As evidenced in Fig. S15a and S15b,† the related images verify that the primary structure of the DSNFSeHS sample was well kept after the longevity test, representing that the DSNFSeHS sample has the desirable longevity. The impressive longevity of the DSNFSeHS electrode can arise from the following reasons: (i) the existence of selenium in the NiFeSe sample can useful for elevating its electrical conductivity and structural durability,[4,22] (ii) the existing porous/hollow space from the spheres can effectively serve as the useful ion buffering reservoirs for reducing the diffusion path to their internal surfaces, and the reaction kinetics can be promoted for better cycling performance.[4,22,30] Also, the coulombic efficiency of the DSNFSeHS (Fig. 5h) and DSNFOHS (Fig. S13†) electrodes retain 96.3% and 93.8% after 10 000 cycles, respectively. From our point of view, the fabulous electrochemical performance of the MSNMSeHS cathode and DSNFSeHS anode electrodes can be justified by their favorable conductivity due to the presence of the Se element in both samples, as well as their exclusive porous textures.

3.6 Construction of the MSNMSeHS||DSNFSeHS device

Motivated by the marvelous performance of the MSNMSeHS cathode and DSNFSeHS anode electrodes, we built an asymmetric apparatus with the MSNMSeHS and DSNFSeHS electrodes. As is evident from the schematic illustration of Fig. 6a, the MSNMSeHS||DSNFSeHS apparatus was well fabricated in a facile manner by sandwiching the MSNMSeHS cathode and DSNFSeHS anode electrodes together with a piece of cellulose paper as a suitable separator in the middle of them to impede a short-circuit. From the CV profiles in the three-electrode cell, the CV area for the optimized DSNFSeHS existed in the potential window range of −1.2 to 0.0 V, and for the MSNMSeHS, it was 0.0 to 0.6 V. Utilizing the maximum potential window of the MSNMSeHS and DSNFSeHS electrodes, our apparatus could be envisaged to deliver the desired potential of 1.8 V (Fig. 6b). To justify the superior performance of the MSNMSeHS||DSNFSeHS-based asymmetric apparatus, we constructed another type of device, in which MSNMSeHS serves as a cathode electrode and activated carbon serves as an anode electrode by holding the condition constant, and the electrochemical tests were conducted for both devices. Fig. 6c reveals the CV plots of the MSNMSeHS||DSNFSeHS, as well as the MSNMSeHS||AC device at 50 mV s^{-1}. As is reflected from these plots, the MSNMSeHS||DSNFSeHS device provided a broader potential window and higher peak current than the MSNMSeHS||AC device, suggesting its superior energy-storage capacity. The CV profiles of the MSNMSeHS||DSNFSeHS device at varying scan speeds starting from 10 to 50 mV s^{-1} did not illustrate any substantial alteration in nature and shape, manifesting the splendid rate capability because of the efficient electron/ion transport kinetics on the active electrodes (Fig. 6d). Besides, the CVs of the MSNMSeHS||AC device at the same scan speeds of 10 to 60 mV s^{-1} are represented in Fig. S16a.† As specified in Fig. S16a,† the CV curves of the MSNMSeHS||AC device display the combined EDLC nature from the activated carbon and battery-type trend from the MSNMSeHS electrode. GCD tests were done to evaluate the cycle life, rate capability, and specific capacity of the constructed devices. Fig. 6e displays GCD profiles of the MSNMSeHS||DSNFSeHS device at diverse current values (1–32 A g^{-1}). GCD plots of the MSNMSeHS||DSNFSeHS exhibited a symmetric nature, indicating the outstanding coulombic efficiency and desirable electrochemical reversibility, which is in accordance with the obtained CV data. Also, at all current densities, the MSNMSeHS||DSNFSeHS device presented a non-linear GCD nature, and followed a battery-type redox mechanism due to the battery-type nature of positive and negative electrodes. For the MSNMSeHS||AC device (Fig. S16b†), the contribution from both battery-type and EDLC behaviors can be clearly seen at all current densities. The MSNMSeHS||DSNFSeHS device showed splendid capacities as high as ~125.1 mA h g^{-1} (450.36 C g^{-1}), 118.25 mA h g^{-1} (425.7 C g^{-1}), 107.35 mA h g^{-1} (386.46 C g^{-1}), 97.9 mA h g^{-1} (352.45 C g^{-1}), and 89.8 mA h g^{-1} (323.3 C g^{-1}) at 1, 4, 8, 16, and 32 A g^{-1} (Fig. 6f). Besides, the related capacities of the MSNMSeHS||AC were found to be 76.45 mA h g^{-1} (275.2 C g^{-1}), 71.9 mA h g^{-1} (258.85 C g^{-1}), 64.17 mA h g^{-1} (231.01 C g^{-1}), 55.8 mA h g^{-1} (200.9 C g^{-1}), and 49.55 mA h g^{-1} (178.4 C g^{-1}) at 1, 4, 8, 16, and 32 A g^{-1}, respectively. Hence, the capacity retention of the MSNMSeHS||DSNFSeHS (71.8% at 32 A g^{-1}) device is considerably higher than that of MSNMSeHS||AC (64.8% at 32 A g^{-1}). Long-term durability is another principal factor for our devices, and was evaluated at 32 A g^{-1} over 10 000 repetitive GCD cycles. For the MSNMSeHS||AC device, the capacity fades to 45.88 mA h g^{-1} (165.2 C g^{-1}) (Fig. S16c†) after the longevity test, corresponding to just 92.6% cycling retention.

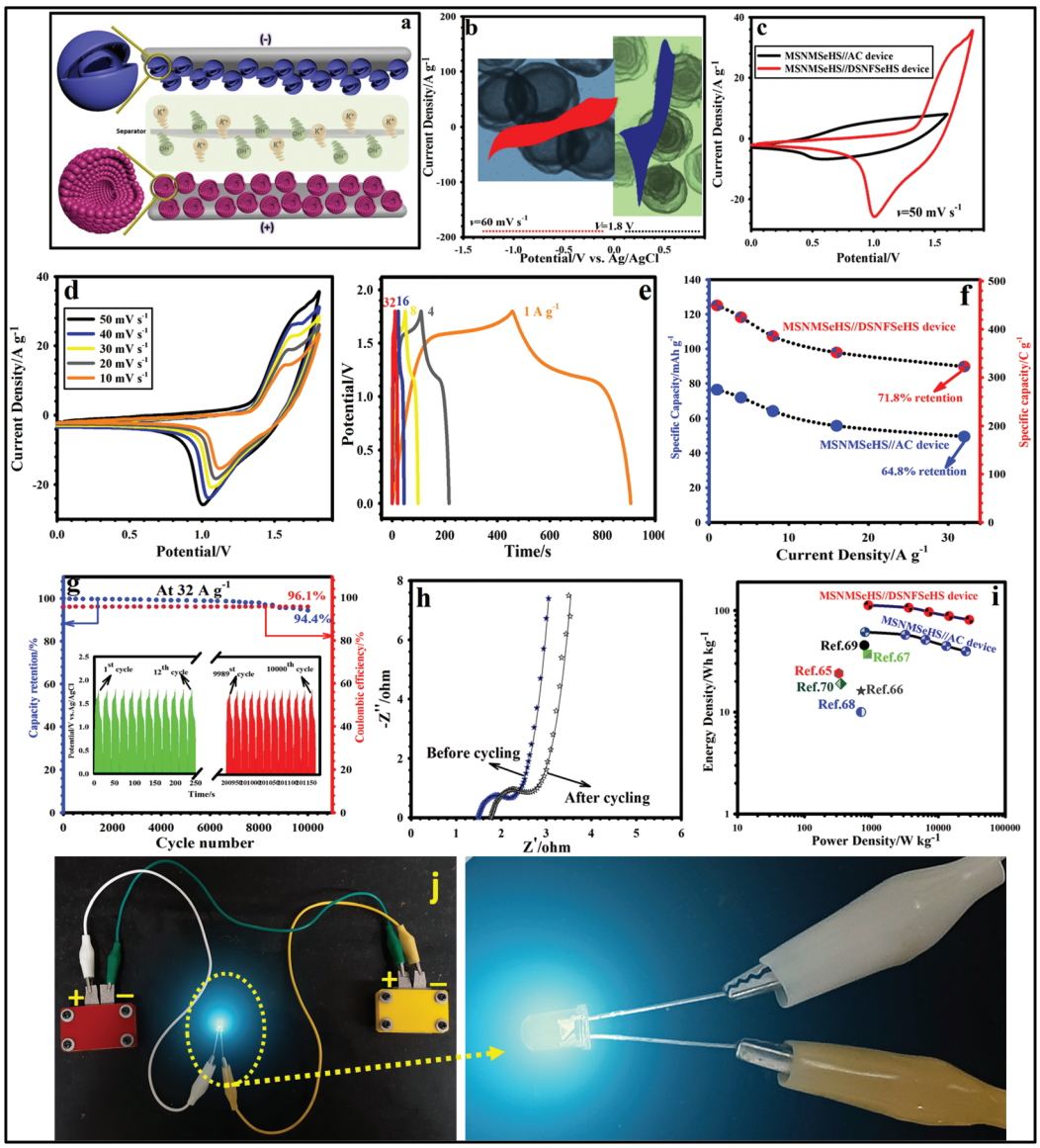

Fig. 6 (a) Schematic showing the MSNMSeHS||DSNFSeHS device. (b) CV plots of the MSNMSeHS (cathode) and DSNFSeHS (anode) electrodes at a scan rate of 60 mV s^{-1}. (c) CV curves of the MSNMSeHS||DSNFSeHS and MSNMSeHS||AC devices at 50 mV s^{-1}. (d) CV plots of the MSNMSeHS||DSNFSeHS device at various sweep rates. (e) GCD profiles of the MSNMSeHS||DSNFSeHS device at various current densities. (f) Rate capability of the MSNMSeHS||DSNFSeHS and MSNMSeHS||AC devices. (g) Cyclability and coulombic efficiency of the MSNMSeHS||DSNFSeHS device. (h) Nyquist plots of the MSNMSeHS||DSNFSeHS device before and after cycling. (i) The comparison of the Ragone plot of the MSNMSeHS||DSNFSeHS device with some reports. (j) Photograph of the blue LED with two devices connected in series.

Nevertheless, for MSNMSeHS||DSNFSeHS (Fig. 6g), the capacity retention was improved to 94.4%, signifying the cycling durability improvement. The GCD profiles of the MSNMSeHS||DSNFSeHS device (inset of Fig. 6g) and MSNMSeHS||AC device (inset of Fig. S16c†) for the initial and last 12 cycles were collected. In comparison to the initial 12 GCD cycles, the ultimate 12 cycles depict small changes in the discharge time, which confirm that both devices hold good longevity. For further exploring the considerable longevity of the MSNMSeHS||DSNFSeHS device, an EIS test was applied before and after the longevity test. As evidenced in Fig. 6h, no notable changes in the R_{ct} value or R_s value are noted, which definitely parallels the splendid longevity of the MSNMSeHS||DSNFSeHS device. Moreover, the coulombic efficiency of the MSNMSeHS||DSNFSeHS device (Fig. 6g) and MSNMSeHS||AC device (Fig. S16c†) holds about 96.1% and 93.3% after 10 000 cycles, respectively. Fig. 6i reveals a Ragone plot of the fabricated MSNMSeHS||DSNFSeHS device. The highest energy density of the MSNMSeHS||DSNFSeHS attains up to 112.6 W h kg^{-1} at 900.8 W kg^{-1}, which is substantially higher than that for the MSNMSeHS||AC device (61.15 W h kg^{-1} at 804.6 W kg^{-1}), and also better than those of the already reported devices (Table S1† and Fig. 6i).[65–70] Moreover, the MSNMSeHS||DSNFSeHS device holds 71.8% of the energy

density (80.84 W h kg^{-1}) retained at 28 871.42 W kg^{-1}, which is higher than that for the MSNMSeHS||AC device (64.8% of the energy density ~39.64 W h kg^{-1} retention at 25 740.25 W kg^{-1}). For checking the practical applications of the MSNMSeHS||DSNFSeHS device, two MSNMSeHS||DSNFSeHS devices were connected in series and then used to power a blue light-emitting diode (LED), as evidenced in Fig. 6j. Hence, all of these outstanding results prove that the constructed MSNMSeHS||DSNFSeHS device is an encouraging system for energy storage applications.

4. Conclusions

In conclusion, we have established a universal and straightforward strategy to design multi-shelled nickel–manganese selenide hollow spheres (MSNMSeHS) and double-shelled nickel–iron selenide hollow spheres (DSNFSeHS) with a manageable shell number as the cathode and anode electrode materials, respectively, for the high-energy-density asymmetric device. The individual cathode and anode electrodes showed splendid electrochemical performance in a three-electrode cell. This fabulous performance in both electrodes has been shown to be due to the high electrical conductivity provided by Se, their special architectures with the highly porous skeleton, and their favorable specific surface areas. An efficient asymmetric apparatus (MSNMSeHS||DSNFSeHS) developed using these two new electrodes displayed an incredible energy density of 112.6 W h kg^{-1} at 900.8 W kg^{-1}, along with considerable longevity of 96.1% capacity maintenance after 10 000 repetitive cycles, which are better than the MSNMSeHS||AC device. Thus, the current research proposes a universal and facile strategy for the development of complex hollow structured mixed metal selenides with promising potential in energy storage devices.

Conflicts of interest

The authors declare no competing financial interest.

Acknowledgements

The authors gratefully acknowledge the support of this work by the Research Councils of Shahid Beheshti University.

References

1 C. Guan, W. Zhao, Y. Hu, Q. Ke, X. Li, H. Zhang and J. Wang, *Adv. Energy Mater.*, 2016, **6**, 1601034.
2 C. Zhu, Y. Ma, W. Zang, C. Guan, X. Liu, S. J. Pennycook, J. Wang and W. Huang, *Chem. Eng. J.*, 2019, **369**, 988.
3 B. Ameri, A. Mohammadi Zardkhoshoui and S. S. Hosseiny Davarani, *Sustainable Energy Fuels*, 2020, **4**, 5144–5155.
4 A. Mohammadi Zardkhoshoui and S. S. Hosseiny Davarani, *Nanoscale*, 2020, **12**, 12476–12489.
5 Z. Yu, L. Tetard, L. Zhai and J. Thomas, *Energy Environ. Sci.*, 2015, **8**, 702–730.
6 T. Shu, H. Gao, Q. Li, F. Wei, Y. Ren, Z. Sun, J. Qi and Y. Sui, *Nanoscale*, 2020, **12**, 20710–20718.
7 A. Mohammadi Zardkhoshoui and S. S. Hosseiny Davarani, *Chem. Eng. J.*, 2020, **402**, 126241.
8 M. Zhu, J. Tang, W. Wei and S. Li, *Mater. Chem. Front.*, 2020, **4**, 1105–1149.
9 A. Mohammadi Zardkhoshoui, R. Hayati Monjoghtapeh and S. S. Hosseiny Davarani, *Energy Fuels*, 2020, **34**(11), 14934–14947.
10 A. Mohammadi Zardkhoshoui and S. S. Hosseiny Davarani, *Nanoscale*, 2020, **12**, 1643–1656.
11 A. Mohammadi Zardkhoshoui, S. S. Hosseiny Davarani, M. Maleka Ashtiani and M. Sarparast, *ACS Sustainable Chem. Eng.*, 2019, **78**, 7908–7917.
12 Q. Yin, H. Jia, A. Mohamed, Q. Ji and L. Hong, *Nanoscale*, 2020, **12**, 5507–5520.
13 L. Zheng, J. Song, X. Ye, Y. Wang, X. Shi and H. Zheng, *Nanoscale*, 2020, **12**, 13811–13821.
14 G. Zhang, X. Xiao, B. Li, P. Gu, H. Xue and H. Pang, *J. Mater. Chem. A*, 2017, **5**, 8155–8186.
15 P. Kulkarni, S. K. Nataraj, R. G. Balakrishna, D. H. Nagaraju and M. V. Reddy, *J. Mater. Chem. A*, 2017, **5**, 22040–22094.
16 Y. Wang, W. Zhang, X. Guo, K. Jin, Z. Chen, Y. Liu, L. Yin, L. Li, K. Yin, L. Sun and Y. Zhao, *ACS Appl. Mater. Interfaces*, 2019, **11**, 7946–7953.
17 B. Kirubasankar, V. Murugadoss, J. Lin, T. Ding, M. Dong, H. Liu, J. Zhang, T. Li, N. Wang, Z. Guo and S. Angaiah, *Nanoscale*, 2018, **10**, 20414–20425.
18 C. Ji, F. Liu, L. Xu and S. Yang, *J. Mater. Chem. A*, 2017, **5**, 5568–5576.
19 Q. Wang, Y. Ma, X. Liang, D. Zhang and M. Miao, *J. Mater. Chem. A*, 2018, **6**, 10361–10369.
20 S. Wei, C. Wan, Y. Jiao, X. Li, J. Li and Y. Wu, *Chem. Commun.*, 2020, **56**, 340–343.
21 T. T. Nguyen, J. Balamurugan, V. Aravindan, N. H. Kim and J. H. Lee, *Chem. Mater.*, 2019, **31**, 4490–4504.
22 J. Balamurugan, T. T. Nguyen, V. Aravindan, N. H. Kim, S. H. Lee and J. H. Lee, *Nano Energy*, 2019, **65**, 103999.
23 X. Shi, H. Wang, S. Ji, V. Linkov, F. Liu and R. Wang, *Chem. Eng. J.*, 2019, **364**, 320–327.
24 X. Tang, Y. H. Lui, B. Zhang and S. Hu, *J. Power Sources*, 2020, **477**, 228977.
25 U. N. Pan, V. Sharma, T. Kshetri, T. I. Singh, D. R. Paudel, N. H. Kim and J. H. Lee, *Small*, 2020, **16**, 2001691.
26 Y. Wang, A. Pan, Y. Zhang, J. Shi, J. Lin, S. Liang and G. Cao, *J. Mater. Chem. A*, 2018, **6**, 9153–9160.
27 A. Mohammadi Zardkhoshoui, M. M. Ashtiani, M. Sarparast and S. S. Hosseiny Davarani, *J. Power Sources*, 2020, **450**, 227691.
28 W. Feng, G. Liu, P. Wang, J. Zhou, L. Gu, L. Chen, X. Li, Y. Dan and X. Cheng, *ACS Appl. Energy Mater.*, 2020, **3**, 7284–7293.

29 Y. Guo, C. Wu, N. Li, S. Yuan and L. Yu, *J. Mater. Chem. A*, 2019, **7**, 25247–25253.
30 Z. Wang, H. Jia, Y. Cai, C. Li, X. Zheng, H. Liang, J. Qi, J. Cao, J. Feng and W. Fei, *Chem. Eng. J.*, 2020, **392**, 123890.
31 H. Tang, M. Zheng, Q. Hu, Y. Chi, B. Xu, S. Zhang, H. Xue and H. Pang, *J. Mater. Chem. A*, 2018, **6**, 13999–14024.
32 Q. Yang, Y. Liu, C. Deng, M. Yan and W. Shi, *J. Mater. Chem. A*, 2019, **7**, 26131–26138.
33 S. Karade, S. Lalwani, J. Eum and H. Kim, *Sustainable Energy Fuels*, 2020, **4**, 3066–3076.
34 C. Guo, Y. Zhang, M. Yin, J. Shi, W. Zhang, X. Wang, Y. Wu, J. Ma, D. Yuan and C. Jia, *J. Power Sources*, 2021, **485**, 229315.
35 X. Qi, W. Zheng, G. He, T. Tian, N. Du and L. Wang, *Chem. Eng. J.*, 2017, **309**, 426–434.
36 J. Guo, Z. Yin, X. Zang, Z. Dai, Y. Zhang, W. Huang and X. Dong, *Nano Res.*, 2017, **10**, 405–414.
37 X. Li, L. Wang, J. Shi, N. Du and G. He, *ACS Appl. Mater. Interfaces*, 2016, **8**, 17276–17283.
38 X. Sun, J. Liu and Y. Li, *Chem. – Eur. J.*, 2006, **12**, 2039–2047.
39 C. Zhu, H. Wang and C. Guan, *Nanoscale Horiz.*, 2020, **5**, 1188–1199.
40 Y. Wang, T. Zhu, Y. Zhang, X. Kong, S. Liang, G. Cao and A. Pan, *J. Mater. Chem. A*, 2017, **5**, 18448–18456.
41 B. Zhou, X. Yang, Y. Sui, G. Xiao, Y. Wei and B. Zou, *Nanoscale*, 2016, **8**, 8784–8790.
42 B. K. Deka, A. Hazarika, S. Lee, D. Y. Kim, Y.-B. Park and H. W. Park, *Nano Energy*, 2020, **73**, 104754.
43 S. Wang, Y. Li, D. Yan, Y. Zou, C. Xie, Y. Wang and Y. Zhang, *J. Mater. Chem. A*, 2017, **5**, 25494–25500.
44 K. Tao, Y. Gong and J. Lin, *Nano Energy*, 2019, **55**, 65–81.
45 A. K. Das, S. Paria, A. Maitra, L. Halder, A. Bera, R. Bera, S. K. Si, A. De, S. Ojha, S. Bera and K. Karan, *ACS Appl. Electron. Mater.*, 2019, **1**, 977–990.
46 X. Wang, X. Zhao, C. Ma, Z. Yang, G. Chen, L. Wang, H. Yue, D. Zhang and Z. Sun, *J. Mater. Chem. A*, 2020, **8**, 1212–1220.
47 J. Deng, X. Huang, W. Gao, H. Liu and M. Xu, *Sustainable Energy Fuels*, 2020, **4**, 4807–4813.
48 J. Li, J. Zhao, R. Tang, Q. Chen, Z. Niu, M. Li, C. Guo, J. Su and L. Zhang, *J. Power Sources*, 2020, **449**, 227517.
49 Y. Xiao, J.-Y. Hwang, I. Belharouak and Y.-K. Sun, *ACS Energy Lett.*, 2017, **2**, 364–372.
50 H. Fan, H. Yu, Y. Zhang, J. Guo, Z. Wang, H. Wang, N. Zhao, Y. Zheng, C. Du, Z. Dai, Q. Yan and J. Xu, *Energy Storage Mater.*, 2018, **10**, 48–55.
51 X. Zheng, X. Han, H. Liu, J. Chen, D. Fu, J. Wang, C. Zhong, Y. Deng and W. Hu, *ACS Appl. Mater. Interfaces*, 2018, **10**, 13675–13684.
52 K. Guo, F. Yang, S. Cui, W. Chen and L. Mi, *RSC Adv.*, 2016, **6**, 46523–46530.
53 Y. Yuan, R. Chen, H. Zhang, Q. Liu, J. Liu, J. Yu, C. Wang, Z. Sun and J. Wang, *Electrochim. Acta*, 2019, **294**, 325–336.
54 L. Yang, X. Lu, S. Wang, J. Wang, X. Guan, X. Guan and G. Wang, *Nanoscale*, 2020, **12**, 1921–1938.
55 L. Wang, R. Zhang, Y. Jiang, H. Tian, Y. Tan, K. Zhu, Z. Yu and W. Li, *Nanoscale*, 2019, **11**, 13894–13902.
56 Y. Liu, Y. Zheng, Q. Xu, Y. Shi, Z. Tian, R. Wang, G. Zhang, J. Chen, Z. Wang and W. Zheng, *Chem. Eng. J.*, 2020, **387**, 124121.
57 H. Chen, M. Fan, C. Li, G. Tian, C. Lv, D. Chen, K. Shu and J. Jiang, *J. Power Sources*, 2016, **329**, 314–322.
58 V. Raman, D. Chinnadurai, R. Rajmohan, V. T. Chebrolu, V. Rajangam and H.-J. Kim, *New J. Chem.*, 2019, **43**, 12630–12640.
59 J. Bhagwan, S. K. Hussain and J. S. Yu, *ACS Sustainable Chem. Eng.*, 2019, **7**, 12340–12350.
60 B. Ramulu, G. Nagaraju, S. C. Sekhar, S. K. Hussain, D. Narsimulu and J. S. Yu, *ACS Appl. Mater. Interfaces*, 2019, **11**, 41245–41257.
61 X. Zhang, F. Yang, H. Chen, K. Wang, J. Chen, Y. Wang and S. Song, *Small*, 2020, **16**, 2004188.
62 A. Mohammadi Zardkhoshoui and S. S. Hosseiny Davarani, *Dalton Trans.*, 2020, **49**, 10028–10041.
63 S. Chen, C. Lu, L. Liu, M. Xu, J. Wang, Q. Deng, Z. Zeng and S. Deng, *Nanoscale*, 2020, **12**, 1852–1863.
64 C. Jiao, Z. Wang, X. Zhao, H. Wang, J. Wang, R. Yu and D. Wang, *Angew. Chem., Int. Ed.*, 2019, **58**, 996–1001.
65 Q. Zhang, W.-B. Zhang, P. Hei, Z. Hou, T. Yang and J. Long, *Appl. Surf. Sci.*, 2020, **527**, 146682.
66 X. Zhang, S. Hou, Z. Ding, G. Zhu, H. Tang, Y. Hou, T. Lu and L. Pan, *J. Alloys Compd.*, 2020, **822**, 153578.
67 X. Wang, C. Jing, W. Zhang, X. Wang, X. Liu, B. Dong and Y. Zhang, *Appl. Surf. Sci.*, 2020, **532**, 147437.
68 S. Gayathri, P. Arunkumar and J. H. Han, *J. Colloid Interface Sci.*, 2021, **582**, 1136–1148.
69 T. Dang, D. Wei, G. Zhang, L. Wang, Q. Li, H. Liu, Z. Cao, G. Zhang and H. Duan, *Electrochim. Acta*, 2020, **341**, 135988.
70 Y. Hu, M. Liu, Q. Yang, L. Kong and L. Kang, *J. Energy Chem.*, 2017, **26**, 49–55.